Global Trajectory-tracking Control for a Tailsitter Flying Wing in Agile Uncoordinated Flight

Ezra Tal* and Sertac Karaman†
Massachusetts Institute of Technology, Cambridge, MA, 02139

We propose a novel control law for accurate tracking of agile trajectories using a tailsitter flying wing micro unmanned aerial vehicle (UAV) that transitions between vertical take-off and landing (VTOL) and forward flight. Our global control formulation enables agile maneuvering throughout the flight envelope, including uncoordinated flight conditions with sideslip. We derive a differential flatness transform for the nonlinear tailsitter dynamics with a simplified aerodynamics model. Using this transform, the proposed controller incorporates accurate tracking of the position reference along with its temporal derivatives velocity, acceleration and jerk, as well as the yaw reference and yaw rate. The inclusion of jerk and yaw rate references through an angular velocity feedforward term increases tracking performance on agile trajectories with fast-changing accelerations. The control design is based on a simplified aerodynamics model that does not require extensive modeling of the aircraft dynamics. By applying incremental nonlinear dynamic inversion (INDI), the controller only depends on a local input-output relation to incrementally update control inputs, resulting in robustness against modeling inaccuracies. We achieve INDI with nonlinear dynamics inversion based on the derived differential flatness transform. The resulting control algorithm is extensively evaluated in flight tests, where it demonstrates accurate trajectory tracking and challenging agile maneuvers, such as uncoordinated sideways flight, aggressive transitions while turning, and differential thrust turning.

Supplemental Material

A video of the experiments can be found at `https://youtu.be/tGQO-6DPT1M`.

I. Introduction

Transitioning powered-lift aircraft combine the vertical take-off and landing (VTOL) and hover capabilities of rotorcraft with the speed and endurance of fixed-wing aircraft. Lift is generated by a powered rotor during take-off, landing and hover flight, while a non-rotating wing generates lift during horizontal flight. There exist various design configurations that achieve powered lift. An aircraft may be equipped with dedicated lift rotors that are stopped once sufficient lift is generated by the wing. Alternatively, the orientation of the rotors may be changed from horizontally spinning to propeller configuration after take-off, like on tiltrotor and tiltwing aircraft. Tailsitter aircraft, on the other hand, rotate in their entirety during transition, so that their rotors transition between lift generation and propulsion based on the attitude of the vehicle.

While the large attitude envelope of tailsitter aircraft may render them less suitable for manned flight, their relative mechanical simplicity makes them an appealing option for unmanned aerial vehicle (UAV) applications. Tailsitter aircraft can exceed the range and endurance limitations typical of multicopters, without sacrificing the capability to take-off, hover, and land in confined spaces. This combination is relevant to many applications. For example, in search and rescue, an unmanned tailsitter aircraft could quickly reach remote locations using horizontal flight, and inspect structures or enter buildings in hovering flight.

A tailsitter flying wing is a tailsitter aircraft without fuselage, tail, and vertical stabilizers or control surfaces. Forgoing these structures simplifies the aerodynamic and mechanical design of the aircraft and potentially improves performance by lowering mass and aerodynamic drag. Due to the lack of vertical aerodynamic surfaces, flying wing aircraft often require active directional stabilization. The fast and relatively powerful brushless motors found on many UAVs are particularly suitable to fulfill this task through differential thrust. By placing flaps that act as elevator and

*Graduate Student, Department of Aeronautics and Astronautics, and Laboratory for Information and Decision Systems, AIAA Student Member.
†Associate Professor of Aeronautics and Astronautics, Laboratory for Information and Decision Systems, AIAA Senior Member.

aileron, i.e., *elevons*, in the rotor wash, the aircraft remains controllable throughout its flight envelope, including static hover conditions. The reduced stability of flying wing aircraft also make them highly maneuverable. Specifically, the lack of vertical surfaces enables maneuvers such as fast skidding turns, and knife edge flight where the wing is pointed in the direction of travel. In general, it permits uncoordinated flight, where the vehicle incurs nonzero lateral velocity.

In this paper, we propose a novel flight control algorithm that is specifically designed for tracking of agile trajectories using the tailsitter flying wing aircraft shown in Fig. 1. The proposed controller uses differential flatness to track the reference position, velocity, acceleration, and jerk (the third derivative of position), as well as yaw angle and yaw rate. It is based on a global formulation, without mode switching or blending, and able to exploit the entire flight envelope, including uncoordinated flight conditions, for agile maneuvering. We derive the controller based on a simplified aerodynamics model [1] and apply incremental nonlinear dynamic inversion (INDI) to achieve accurate trajectory tracking despite model discrepancies.

Differential flatness is a property of nonlinear dynamics systems that guarantees the existence of an equivalent controllable linear system [2–4]. The state variables and control inputs of a flat system can be expressed as the function of a (ficticious) flat output and a finite number of its time-derivatives. Using this function, trajectories can be generated in the flat output space and transformed to the state space for tracking control [5, 6]. This enables tracking higher-order derivatives of the output, which has been demonstrated to improve trajectory-tracking performance in fast and agile flight [7–10]. The differential flatness property has been shown to hold for idealized aircraft dynamics [11], and for aggressive fighter maneuvers in coordinated flight. [12]

Incremental, or sensor-based, nonlinear dynamic inversion is a version of nonlinear dynamic inversion (NDI) control that alleviates the lack of robustness associated with NDI [13] by incrementally updating control inputs based on inertial measurements. [14, 15] Instead of directly computing control inputs from the inverted dynamics model, it only considers the input-output relation around the current operating point and computes the required control increment relative to this point. [16] As such, it only relies on local accuracy of the dynamics model and can correct for discrepancies by further incrementing control inputs in subsequent updates.

Existing flight control designs for tailsitter aircraft are based on various approaches. Blending of separate controllers [17], gain scheduling [18], or pre-planned transition maneuvers [19] can be used to handle the change of dynamics between hover and forward flight. However, when performing agile maneuvering at large angle of attack, the aircraft continuously enters and exits the transition regime and it is preferable to utilize a controller without blending or switching. A global formulation for trajectory tracking in coordinated flight is proposed by [20]. The controller is based on numerical inversion of a global first-principles model, but does not account for model discrepancies, leading to a systematic pitch tracking error. Wind tunnel testing can be used to improve accuracy of the dynamics model [21, 22]. However, building an accurate model from measurements can be a time-consuming process that may need to be repeated if the controller is transferred to a different vehicle. The controller proposed by [23] uses the ϕ-theory simplified aerodynamics model proposed by [1] that is also used in our proposed control algorithm. Their design accounts for model discrepancies by applying model-free control. INDI has also been applied for robust control of tiltrotor [24] and tailsitter [25] transitioning aircraft. Our control design differs from existing INDI controllers in several ways. We focus on tracking of agile trajectories, while existing works enforce coordinated flight at small flight path angles and do not employ differential flatness to accomplish jerk tracking. Additionally, flatness enables nonlinear inversion of our dynamics model, while existing INDI implementations rely on local linearization to obtain inversion. The algorithm by [26] makes use of flatness to design transition maneuvers for a quadrotor biplane, but only considers simplified longitudinal dynamics. The resulting trajectories consider acceleration, but no higher-order derivatives. The controller by [22] employs a pre-designed constant angular velocity feedforward input to improve transition. Theoretically, this feedforward signal corresponds to the acceleration rate of change, i.e., jerk. However, it is not applied beyond the pre-designed transition maneuver.

The main contribution of this paper is a global control design for tracking agile trajectories using a flying wing tailsitter. Our proposed control design is novel in several ways. Firstly, we derive a differential flatness transform for the tailsitter flight dynamics with simplified ϕ-theory aerodynamics model. Secondly, we present a method to incorporate jerk tracking as a angular velocity feedforward input in tailsitter control design. As far as we are aware, this is the first tailsitter controller that achieves jerk tracking, making it suitable to fly agile trajectories with fast-changing acceleration references. Thirdly, we apply INDI to control a tailsitter aircraft in agile maneuvers that include large flight path angles and uncoordinated flight conditions. Our INDI control design is based on direct nonlinear inversion and contrary to existing implementations does not rely on linearization of the dynamics for inversion. Finally, we demonstrate the proposed controller in extensive flight experiments reaching up to 8 m/s in an indoor flight space measuring 18 m $\times$ 8 m. The flight experiments include agile maneuvers, such as aggressive transitions while turning, differential thrust turning,

Fig. 1 Tailsitter flying wing aircraft.

and uncoordinated flight.

This paper is structured as follows: In Section II, we provide a overview of the flight dynamics and aerodynamics model. We derive the differential flatness transform that is used to compute the attitude command and angular velocity feedforward input in Section III. The design of the trajectory-tracking controller is presented in Section IV, and experimental results are shown in Section V. Finally, conclusions are provided in Section VI.

II. Flight Dynamics Model

This section provides a detailed overview of the flight dynamics model employed in our proposed control algorithm. The algorithm, described in Section IV, is based on the notion of incremental control action and therefore utilizes the dynamics model solely as a local approximation of the flight dynamics. Unlike conventional inversion-based controllers, it does not require a globally accurate dynamics model.

The model is employed by the incremental controller to predict (i) the change in linear acceleration due to increments in attitude and collective thrust, and (ii) the change in angular acceleration due to increments in differential thrust and flap deflections. By inversion of these relationships, the control algorithm computes the increments required to attain the commanded changes in linear and angular acceleration. In order to maintain analytical invertibility and avoid undue complexity, the dynamics model omits any contributions that do not directly affect the aforementioned incremental relationships. For example, the velocity of the aircraft relative to the atmosphere may result in a significant aerodynamic moment. However, when compared to the fast dynamics of the motors and servos controlling the propellers and flaps, this moment contribution is relatively slow-changing, as it relates to the orientation and velocity of the entire vehicle. Consequently, it is assumed to be constant between control updates and does not need to be included in the incremental dynamics model. It is nonetheless accounted for in the control algorithm together with other unmodeled contributions to linear and angular acceleration through inertial measurement feedback, as described in Section IV.

A. Reference Frame Conventions

Figure 2 depicts the world and body-fixed reference frames used in the dynamics model and flight controller. The basis of the world-fixed north-east-down (NED) reference frame consists of the columns of the identity matrix $[\mathbf{i}_x\ \mathbf{i}_y\ \mathbf{i}_z]$. We define the basis of the body-fixed reference frame as the vectors $\mathbf{b}_x$ which coincides with the chord line and the wing symmetry plane, $\mathbf{b}_y$ which is perpendicular to this symmetry plane, and $\mathbf{b}_z$ which is defined to satisfy the right-hand rule. These vectors form the rotation matrix $\mathbf{R}_b^i = [\mathbf{b}_x\ \mathbf{b}_y\ \mathbf{b}_z] \in SO(3)$, which gives the transformation from the body-fixed

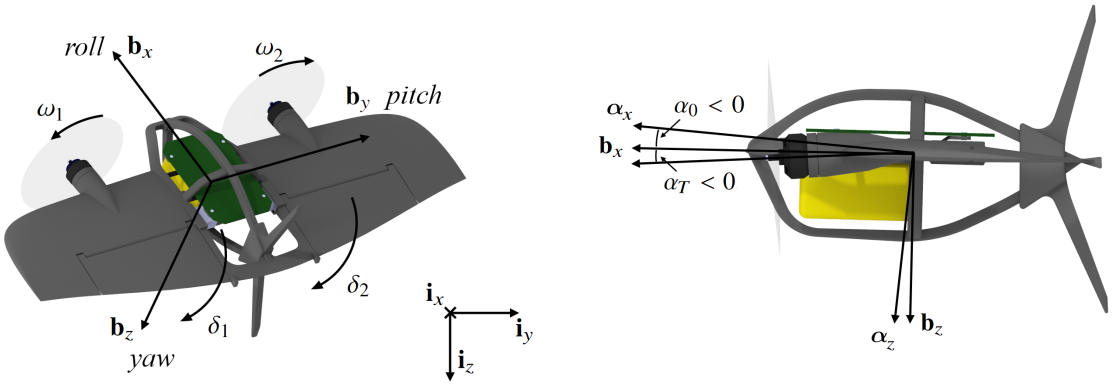

(a) Body-fixed reference frame, control inputs, and angular motion terminology.

(b) Zero-lift reference frame, zero-lift angle of attack, and thrust angle.

Fig. 2 Reference frame and control input conventions.

reference frame (indicated by the subscript b) to the world-fixed reference frame (indicated by the superscript i). To avoid confusion when referring to rotations in the body-fixed reference frame, we use the terms in Fig. 2a irrespective of vehicle orientation. We note that the term *yaw* is also used to refer to rotation around the world-fixed $\mathbf{i}_z$-axis in the context of the reference trajectory defined in Section III.

The zero-lift axis system, depicted in Fig. 2b, is obtained by rotating the body-fixed axis system around its negative $\mathbf{b}_y$-axis by the zero-lift angle of attack α_0, which is defined as the angle of attack for which the aircraft produces zero lift. For symmetric airfoils $\alpha_0 = 0$, while most cambered airfoils have $\alpha_0 < 0$. Finally, the thrust angle α_T is defined as the angle of the thrust line with regard to the $\mathbf{b}_x$-$\mathbf{b}_y$ plane. Typically, motors are slightly tilted down, leading to $\alpha_T < 0$.

B. Vehicle Equations of Motion

The vehicle translational dynamics are given by

$$\dot{\mathbf{x}} = \mathbf{v}, \tag{1}$$

$$\dot{\mathbf{v}} = g\mathbf{i}_z + m^{-1}\left(\mathbf{R}_\alpha^i \mathbf{f}^\alpha + \mathbf{f}_{\text{ext}}\right), \tag{2}$$

where $\mathbf{x}$ and $\mathbf{v}$ are respectively the vehicle position and velocity in the world-fixed reference frame, g is the gravitational acceleration, and m is the vehicle mass. The vector $\mathbf{f}^\alpha$ represents the modeled aerodynamic and thrust force in the zero-lift reference frame. Any unmodeled forces are represented by the external force vector $\mathbf{f}_{\text{ext}}$, which is defined in the world-fixed reference frame.

The rotational dynamics are given by

$$\dot{\boldsymbol{\xi}} = \frac{1}{2}\boldsymbol{\xi} \circ \boldsymbol{\Omega}, \tag{3}$$

$$\dot{\boldsymbol{\Omega}} = \mathbf{J}^{-1}(\mathbf{m} + \mathbf{m}_{\text{ext}} - \boldsymbol{\Omega} \times \mathbf{J}\boldsymbol{\Omega}), \tag{4}$$

where $\boldsymbol{\Omega}$ is the angular velocity in the body-fixed reference frame, and $\boldsymbol{\xi}$ is the normed quaternion attitude vector. The Hamilton quaternion product is denoted by $\circ$, such that $\mathbf{v}^b = \mathbf{R}_i^b \mathbf{v} = \boldsymbol{\xi}^{-1} \circ \mathbf{v} \circ \boldsymbol{\xi}$. The matrix $\mathbf{J}$ is the vehicle moment of inertia tensor, and $\mathbf{m}$ represents the aerodynamic and thrust moment in the body-fixed reference frame. The external moment vector $\mathbf{m}_{\text{ext}}$ represents unmodeled moment contributions, similar to the force vector $\mathbf{f}_{\text{ext}}$. The final term of (4) accounts for the conservation of angular momentum. We note that the term *external* with regard to $\mathbf{f}_{\text{ext}}$ and $\mathbf{m}_{\text{ext}}$ refers to unmodeled force and moment contributions, i.e., external to the model, but not necessarily due to physically external influences, such as gusts.

C. Aerodynamic and Thrust Force and Moment

We employ ϕ-theory parametrization to model the aerodynamic force and moment [1]. This parametrization has several advantages over standard expressions for aerodynamic coefficients. Firstly, it provides a simple global model that includes dominant contributions over the entire flight envelope, including post-stall conditions. Our simplified model relies on only nine scalar aerodynamic coefficients: two for the wing, two for the flaps, two for the propellers, and three for propeller-wing interaction. Secondly, ϕ-theory parametrization avoids the singularities that methods based angle of attack and sideslip angle incur near hover conditions, where these angles are undefined.

We obtain the force in the zero-lift axis system by summing contributions due to thrust, flaps, and wings. The thrust force is given by

$$\mathbf{f}_T^\alpha = \sum_{i=1}^{2} \underbrace{\begin{bmatrix} \cos\bar{\alpha}\,(1-c_{D_T}) \\ 0 \\ \sin\bar{\alpha}\,(c_{L_T}-1) \end{bmatrix} T_i}_{\mathbf{f}_{T_i}^\alpha}, \tag{5}$$

where $\bar{\alpha} = \alpha_0 + \alpha_T$, T_i is the thrust due to motor i, and the coefficients c_{D_T} and c_{L_T} represent drag and lift due to thrust vector components in the zero-lift axis system, respectively. The motor thrust is computed as follows:

$$T_i = c_T \omega_i^2 \quad \text{with} \quad i = 1, 2, \tag{6}$$

where $\omega_i \geq 0$ is the speed of motor i. The thrust coefficient c_T is a function of propeller geometry and can be obtained from bench tests using a force balance. Intuitively, c_{D_T} mostly represents the loss of propeller efficiency due to the presence of the wing in the propwash, while c_{L_T} represents the propwash-induced lift. Note that the lift component vanishes if the thrust line coincides with the zero-lift axis, i.e., $\alpha_0 + \alpha_T = 0$. For convenience, all aerodynamic coefficients incorporate the effects of air density. If the coefficients are applied for flight in significantly varying conditions, their values may be recomputed using a simple scaling with air density. The force contribution by the flaps is given by

$$\mathbf{f}_\delta^\alpha = \sum_{i=1}^{2} \underbrace{-\begin{bmatrix} 0 \\ 0 \\ c_{L_T}^\delta \cos\bar{\alpha}\, T_i + c_{L_V}^\delta \|\mathbf{v}\| \mathbf{i}_x^\top \mathbf{v}^\alpha \end{bmatrix}}_{\mathbf{f}_{\delta_i}^\alpha} \delta_i, \tag{7}$$

where δ_i is the deflection angle of flap i. The first term of (7), scaled with the coefficient $c_{L_T}^\delta$, is the flap lift due to the prop-wash induced airspeed. The second term, scaled with $c_{L_V}^\delta$, is the flap lift due to the airspeed along the zero-lift line. Finally, the wing force contribution is obtained as

$$\mathbf{f}_w^\alpha = -\begin{bmatrix} c_{D_V} \mathbf{i}_x^\top \mathbf{v}^\alpha \\ 0 \\ c_{L_V} \mathbf{i}_z^\top \mathbf{v}^\alpha \end{bmatrix} \|\mathbf{v}\|, \tag{8}$$

where c_{D_V} and c_{L_V} are the wing drag and lift coefficients, respectively. The total force in the zero-lift axis system is now obtained as

$$\mathbf{f}^\alpha = \mathbf{f}_T^\alpha + \mathbf{f}_\delta^\alpha + \mathbf{f}_w^\alpha. \tag{9}$$

We note that (9) does not contain any lateral force component. Due to the lack of a fuselage and vertical tail surface lateral force is relatively much smaller than the lift and drag components. Any incurred lateral force is captured in the unmodeled force $\mathbf{f}_{\text{ext}}$, and accounted for by the controller through accelerometer feedback, as described in Section IV.B.

The moment is obtained by summation of contributions due to motor thrust and torque, and flap deflections. We ignore the wing moment due to velocity, attitude and rotation rates, as these state variables are relatively slow-changing compared to the motor speeds and flap deflections. The corresponding contributions are incorporated in the unmodeled moment $\mathbf{m}_{\text{ext}}$ and accounted for through angular acceleration feedback. The moment due to motor thrust is given by

$$\mathbf{m}_T = \begin{bmatrix} l_{T_y} \mathbf{i}_z^\top \mathbf{R}_\alpha^b (\mathbf{f}_{T_2}^\alpha - \mathbf{f}_{T_1}^\alpha) \\ c_{\mu T}(T_1 + T_2) \\ l_{T_y} \mathbf{i}_x^\top \mathbf{R}_\alpha^b (\mathbf{f}_{T_1}^\alpha - \mathbf{f}_{T_2}^\alpha) \end{bmatrix}, \tag{10}$$

where l_{T_y} is the absolute distance along $\mathbf{b}_y$ between the vehicle center of gravity and each motor, and $c_{\mu T}$ is the pitch moment coefficient due to thrust. The moment due to motor torque is obtained as follows:

$$\mathbf{m}_\mu = \begin{bmatrix} \cos\alpha_T \\ 0 \\ -\sin\alpha_T \end{bmatrix} \sum_{i=1}^{2} \mu_i, \tag{11}$$

where μ_i is the motor torque around the thrust-fixed x-axis given by

$$\mu_i = -(-1)^i c_\mu \omega_i^2 \tag{12}$$

with c_μ the propeller torque coefficient. The signs in (12) correspond to the rotation directions as defined in Fig. 2b. The flap contribution to the aerodynamic moment is given by

$$\mathbf{m}_\delta = \begin{bmatrix} l_{\delta_y} \cos\alpha_0 \, \mathbf{i}_z^\top (\mathbf{f}_{\delta_2}^\alpha - \mathbf{f}_{\delta_1}^\alpha) \\ l_{\delta_x} \mathbf{i}_z^\top (\mathbf{f}_{\delta_1}^\alpha + \mathbf{f}_{\delta_2}^\alpha) \\ l_{\delta_y} \sin\alpha_0 \, \mathbf{i}_z^\top (\mathbf{f}_{\delta_2}^\alpha - \mathbf{f}_{\delta_1}^\alpha) \end{bmatrix}, \tag{13}$$

where l_{δ_y} is the absolute distance between the vehicle center of gravity and each flap center along the $\mathbf{b}_y$ axis, and l_{δ_x} is the distance from this axis to the aerodynamic center of both flaps. The total aerodynamic moment can now be obtained by summing the contributions, as follows:

$$\mathbf{m} = \mathbf{m}_T + \mathbf{m}_\mu + \mathbf{m}_\delta. \tag{14}$$

III. Differential Flatness

The purpose of our control design is to accurately track the trajectory reference

$$\boldsymbol{\sigma}_{\text{ref}}(t) = [\mathbf{x}_{\text{ref}}(t)^T \ \psi_{\text{ref}}(t)]^T, \tag{15}$$

which consists of four elements: The vehicle position in the world-fixed reference frame $\mathbf{x}_{\text{ref}}(t) \in \mathbb{R}^3$, and the yaw angle $\psi_{\text{ref}}(t) \in \mathbb{T}$, where $\mathbb{T}$ denotes the circle group. The reference $\boldsymbol{\sigma}_{\text{ref}}(t)$ may be provided by a pre-planned trajectory, or by an online motion planning algorithm. Henceforward, we do not explicitly write the time argument t everywhere. The position reference $\mathbf{x}_{\text{ref}}$ is at least third-order continuous, and the yaw reference ψ_{ref} is at least first-order continuous. By taking the derivative of $\mathbf{x}_{\text{ref}}$, we obtain continuous references for velocity $\mathbf{v}_{\text{ref}}$, acceleration $\mathbf{a}_{\text{ref}}$, and jerk $\mathbf{j}_{\text{ref}}$. Similarly, we obtain a continuous yaw rate reference $\dot{\psi}_{\text{ref}}$ from the yaw reference ψ_{ref}.

Differential flatness of a nonlinear dynamics system entails the existence of an equivalent controllable linear system via a specific type of feedback linearization. For further details on differential flatness and its applications in general, we refer the reader to [2–4]. An important property of flat systems is that their state and input variables can be directly expressed as a function of the flat output and a finite number of its derivatives. This property is of major importance when developing trajectory generation and tracking algorithms, as it allows one to readily obtain state and input trajectories corresponding to an output trajectory, effectively transforming the output tracking problem into a state tracking problem. In practice, the state trajectory can serve as a feedforward control input that enables tracking of higher-order derivatives of the flat output. Inclusion of these feedforward inputs improves trajectory tracking performance by reducing the phase lag in the response to rapid changes in the flat output.

In this section, we show differential flatness of the dynamics system described in Section II—with some simplifications—by deriving expressions of the state and control inputs as a function of the flat output defined by (15). The expression for angular velocity is used in our trajectory-tracking controller to obtain a feedforward input based on the reference jerk and yaw rate. Expressions for attitude and the control inputs are used for linear and angular acceleration control, respectively.

A. Attitude and Collective Thrust

The position and velocity states are trivially obtained from (15). We arrive at expressions for the attitude and collective thrust by rewriting (2) as

$$\mathbf{f}^i = m\,(\mathbf{a} - g\mathbf{i}_z) - \mathbf{f}_{\text{ext}}, \tag{16}$$

where we assume that $\mathbf{f}_{\text{ext}}$ is constant. In practice $\mathbf{f}_{\text{ext}}$ may not be constant, but it is implicitly estimated and corrected for by incremental control, as described in Section IV.B. Given (16), the vehicle attitude and collective thrust are uniquely defined by three major constraints:

(i) the yaw angle reference ψ,
(ii) the fact that $\mathbf{i}_y^\top \mathbf{f}^\alpha = 0$ according to (5), and
(iii) the forces in the vehicle symmetry plane, i.e., $\mathbf{i}_x^\top \mathbf{f}^\alpha$ and $\mathbf{i}_z^\top \mathbf{f}^\alpha$.

Additionally, we exploit the continuity of yaw and the fact that the collective thrust must be non-negative.

In this section, we express the attitude using Euler angles ψ, ϕ, and θ in ZXY rotation sequence. The angle symbols are also used to refer to rotation matrices between intermediate frames, e.g., the rotation matrix $\mathbf{R}_i^\phi$ represents the rotations by ψ and ϕ. The ZXY Euler angles form a valid and universal attitude representation that is suitable for the flat transform, because each of the angles is uniquely defined by one of the constraints, as shown in Fig. 3. In order to avoid the well-known issues with Euler angles, we convert the obtained attitude to quaternion format before it is used by the flight controller.

We define the yaw angle ψ as the angle between the world-fixed $\mathbf{i}_y$-axis and the projection of the body-fixed $\mathbf{b}_y$-axis onto the horizontal plane, i.e., the plane perpendicular to $\mathbf{i}_z$. While this angle is undefined if the wingtips are pointing straight up/down (i.e., $\mathbf{i}_z^\top \mathbf{b}_y = \pm 1$), we avoid ambiguity by performing the yaw rotation $\psi \mathbf{i}_z$ from the identity rotation (i.e., from $\mathbf{R}_i^b = \mathbf{I}$).

Next, we satisfy constraint (ii) by rotation around the yawed x-axis $\mathbf{R}_\psi^i \mathbf{i}_x$ by

$$\phi = -\operatorname{atan2}\left(\mathbf{i}_y^\top \mathbf{R}_i^\psi \mathbf{f}^i, \mathbf{i}_z^\top \mathbf{f}^i\right) + k\pi, \tag{17}$$

where atan2 is the four-quadrant inverse tangent function. In the second term, $k \in \{0, 1\}$ is set such that $\mathbf{b}_y \bullet \mathbf{R}_\phi^i \mathbf{i}_y > 0$, i.e., such that the obtained y-axis corresponds as closely as possible to the current $\mathbf{b}_y$-axis. This results in the equivalence $\psi \equiv \psi + \pi$, which enables continuous yaw tracking through discontinuities, such as a roll maneuver where the yaw angle instantly switches to $\psi + \pi$. Unwanted switching does not occur due to continuity of the yaw reference. If the commanded force is entirely in the horizontal plane and perpendicular to the yaw direction, both arguments of the tangent function are zero and any ϕ satisfies the constraint. This condition is highly unlikely to occur in actual flight, but can be resolved in practice by setting ϕ to match the current direction of $\mathbf{b}_y$ as closely as possible.

To satisfy constraint (iii), we solve (9) for the collective thrust $T = T_1 + T_2$ and for the rotation angle $\bar{\theta}$ around the vehicle y-axis. In order to find these expressions, we assume that the flap angles are constant and known. We can make this assumption without consequence, because of a limitation of the INDI acceleration controller. As described in Section IV, we only consider the low-frequency component of the flap deflection when controlling the linear acceleration. This slow-changing component is virtually constant between control updates.

Since the individual thrust values are still undetermined, we assume that the difference between the steady-state flap deflections is negligible so that

$$\delta_1 T_1 + \delta_2 T_2 \approx \frac{T}{2}\delta, \tag{18}$$

where $\delta = \delta_1 + \delta_2$. This assumption may be violated during sustained maneuvers or flight with sideslip, but we have found that it typically does not lead to large discrepancies. We substitute into (9) $\mathbf{f}^\alpha = \mathbf{R}_\phi^{\bar{\theta}} \mathbf{f}^\phi$ and $\mathbf{v}^\alpha = \mathbf{R}_\phi^{\bar{\theta}} \mathbf{v}^\phi$ with $\mathbf{f}^\phi = \mathbf{R}_i^\phi \mathbf{f}^i$, $\mathbf{v}^\phi = \mathbf{R}_i^\phi \mathbf{v}^i$. Note that $\bar{\theta}$ refers to the rotation from ϕ to the zero-lift reference frame, while θ is the rotation to the body-fixed reference frame. We obtain the following two equalities:

$$\mathrm{c}\bar{\alpha}\ \left(1 - c_{D_T}\right) T - c_{D_V} \|\mathbf{v}\| \left(\mathrm{c}\bar{\theta}\ \mathbf{i}_x^\top \mathbf{v}^\phi - \mathrm{s}\bar{\theta}\ \mathbf{i}_z^\top \mathbf{v}^\phi\right) = \mathrm{c}\bar{\theta}\ \mathbf{i}_x^\top \mathbf{f}^\phi - \mathrm{s}\bar{\theta}\ \mathbf{i}_z^\top \mathbf{f}^\phi, \tag{19}$$

$$\begin{aligned}\left(\mathrm{s}\bar{\alpha}\ (c_{L_T} - 1) - \mathrm{c}\bar{\alpha}\ c_{L_T}^\delta \delta/2\right) T - c_{L_V}^\delta \delta \|\mathbf{v}\| \left(\mathrm{c}\bar{\theta}\ \mathbf{i}_x^\top \mathbf{v}^\phi - \mathrm{s}\bar{\theta}\ \mathbf{i}_z^\top \mathbf{v}^\phi\right) - c_{L_V} \|\mathbf{v}\| \left(\mathrm{s}\bar{\theta}\ \mathbf{i}_x^\top \mathbf{v}^\phi + \mathrm{c}\bar{\theta}\ \mathbf{i}_z^\top \mathbf{v}^\phi\right) = \\ \mathrm{s}\bar{\theta}\ \mathbf{i}_x^\top \mathbf{f}^\phi + \mathrm{c}\bar{\theta}\ \mathbf{i}_z^\top \mathbf{f}^\phi,\end{aligned} \tag{20}$$

where c and s represent respectively cosine and sine, and $\bar{\alpha} = \alpha_0 + \alpha_T$. Solving (19) and (20) for $\bar{\theta}$ and T gives

$$\begin{aligned}\bar{\theta} = \operatorname{atan2}\Big(&\eta\left(\mathbf{i}_x^\top \mathbf{f}^\phi + c_{D_V} \|\mathbf{v}\| \mathbf{i}_x^\top \mathbf{v}^\phi\right) - c_{L_V}^\delta \delta \|\mathbf{v}\| \mathbf{i}_x^\top \mathbf{v}^\phi - c_{L_V} \|\mathbf{v}\| \mathbf{i}_z^\top \mathbf{v}^\phi - \mathbf{i}_z^\top \mathbf{f}^\phi, \\ &\eta\left(\mathbf{i}_z^\top \mathbf{f}^\phi + c_{D_V} \|\mathbf{v}\| \mathbf{i}_z^\top \mathbf{v}^\phi\right) - c_{L_V}^\delta \delta \|\mathbf{v}\| \mathbf{i}_z^\top \mathbf{v}^\phi + c_{L_V} \|\mathbf{v}\| \mathbf{i}_x^\top \mathbf{v}^\phi + \mathbf{i}_x^\top \mathbf{f}^\phi\Big) + k\pi,\end{aligned} \tag{21}$$

$$T = \frac{1}{\mathrm{c}\bar{\alpha}\ \left(1 - c_{D_T}\right)} \left(\mathrm{c}\bar{\theta}\ \mathbf{i}_x^\top \mathbf{f}^\phi - \mathrm{s}\bar{\theta}\ \mathbf{i}_z^\top \mathbf{f}^\phi + c_{D_V} \|\mathbf{v}\| \left(\mathrm{c}\bar{\theta}\ \mathbf{i}_x^\top \mathbf{v}^\phi - \mathrm{s}\bar{\theta}\ \mathbf{i}_z^\top \mathbf{v}^\phi\right)\right), \tag{22}$$

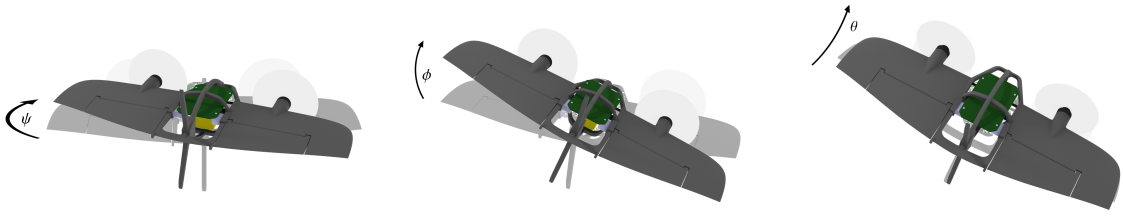

(a) Yaw rotation to satisfy the yaw reference. **(b) Roll rotation to satisfy $\mathbf{i}_y^\top \mathbf{f}^\alpha = 0$.** **(c) Pitch rotation to attain $\mathbf{i}_x^\top \mathbf{f}^\alpha$ and $\mathbf{i}_z^\top \mathbf{f}^\alpha$.**

Fig. 3 Rotation sequence for attitude flatness transform.

where

$$\eta = \frac{\mathrm{s}\bar{\alpha}\ \left(c_{L_T} - 1\right) - \mathrm{c}\bar{\alpha}\ c_{L_T}^{\delta}\,\delta/2}{\mathrm{c}\bar{\alpha}\ \left(1 - c_{D_T}\right)}. \tag{23}$$

is the ratio of lift and forward force due to thrust. We set $k \in \{0, 1\}$ such that $T \geq 0$. In the unlikely event that constraint (iii) is satisfied for any $\bar{\theta}$, both arguments of the atan2 function equal zero and in practice we can set $\bar{\theta}$ to match the current attitude as closely as possible. Since the angle $\bar{\theta}$ is the rotation to the zero-lift axis system, we use $\theta = \bar{\theta} + \alpha_0$ to obtain the corresponding rotation to the body-fixed reference frame.

Note that we purposely selected the ZXY rotation sequence and the definition of yaw, such that ϕ and θ do not affect the satisfaction of constraint (i), and θ does not affect the satisfaction of constraint (ii). Given that the Euler angles are uniquely defined (up to addition of π) by the yaw reference, (17), and (21), this implies that these expressions give the attitude as a function of $\boldsymbol{\sigma}_{\mathrm{ref}}$.

B. Angular Velocity

By taking the derivative of (17), we obtain

$$\dot{\phi} = \frac{\left(\mathrm{c}\psi\ \dot{\psi}\mathbf{i}_x^\top\mathbf{f}^i + \mathrm{s}\psi\ \mathbf{i}_x^\top\dot{\mathbf{f}}^i + \mathrm{s}\psi\ \dot{\psi}\mathbf{i}_y^\top\mathbf{f}^i - \mathrm{c}\psi\ \mathbf{i}_y^\top\dot{\mathbf{f}}^i\right)\mathbf{i}_z^\top\mathbf{f}^i - \left(\mathrm{s}\psi\ \mathbf{i}_x^\top\mathbf{f}^i - \mathrm{c}\psi\ \mathbf{i}_y^\top\mathbf{f}^i\right)\mathbf{i}_z^\top\dot{\mathbf{f}}^i}{\left(\mathbf{i}_y^\top\mathbf{R}_i^\psi\mathbf{f}^i\right)^2 + \left(\mathbf{i}_z^\top\mathbf{f}^i\right)^2}, \tag{24}$$

where the force derivative is obtained as the derivative of (16), as follows:

$$\dot{\mathbf{f}}^i = m\mathbf{j}. \tag{25}$$

We take the derivative of (21) to obtain

$$\dot{\theta} = \frac{\left(\eta\left(\mathbf{i}_x^\top\dot{\mathbf{f}}^\phi + c_{D_V}\tau_x\right) - c_{L_V}^{\delta}\,\delta\tau_x - c_{L_V}\tau_z - \mathbf{i}_z^\top\dot{\mathbf{f}}^\phi\right)\sigma_2 - \sigma_1\left(\eta\left(\mathbf{i}_z^\top\dot{\mathbf{f}}^\phi + c_{D_V}\tau_z\right) - c_{L_V}^{\delta}\,\delta\tau_z + c_{L_V}\tau_x + \mathbf{i}_x^\top\dot{\mathbf{f}}^\phi\right)}{\sigma_1^2 + \sigma_2^2}, \tag{26}$$

where σ_1 and σ_2 are respectively the first and second arguments of the atan2 function in (21), and

$$\tau_x = \|\dot{\mathbf{v}}\|\mathbf{i}_x^\top\mathbf{v}^\phi + \|\mathbf{v}\|\mathbf{i}_x^\top\dot{\mathbf{v}}^\phi, \tag{27}$$

$$\tau_z = \|\dot{\mathbf{v}}\|\mathbf{i}_z^\top\mathbf{v}^\phi + \|\mathbf{v}\|\mathbf{i}_z^\top\dot{\mathbf{v}}^\phi \tag{28}$$

with

$$\|\dot{\mathbf{v}}\| = \frac{\mathbf{v}^\top\mathbf{a}}{\|\mathbf{v}\|}, \tag{29}$$

$$\dot{\mathbf{v}}^\phi = \frac{d}{dt}\left(\mathbf{R}_i^\phi\right)\mathbf{v} + \mathbf{R}_i^\phi\mathbf{a}. \tag{30}$$

The expression for the force derivative $\dot{\mathbf{f}}^{\phi}$ is similar to (30). Finally, we obtain the angular velocity in the body-fixed reference frame, as follows:

$$\boldsymbol{\Omega} = \begin{bmatrix} 0 \\ \dot{\theta} \\ 0 \end{bmatrix} + \mathbf{R}_{\phi}^{\theta} \begin{bmatrix} \dot{\phi} \\ 0 \\ 0 \end{bmatrix} + \mathbf{R}_{\psi}^{\theta} \begin{bmatrix} 0 \\ 0 \\ \dot{\psi} \end{bmatrix}. \tag{31}$$

C. Control Inputs

At this point, we have expressed the state variables as a function of the flat output (15). To obtain an expression for the control inputs, first an expression for angular acceleration is obtained as the derivative of (31) and substituted into (4) to obtain an expression for $\mathbf{m}$. The angular acceleration can be utilized as a feedforward input corresponding to snap, the fourth derivative of position [10]. However, calculation of this feedforward input significantly complicates the controller expressions, and its benefit may be marginal given how challenging it is to accurately control angular acceleration on an aircraft. Hence, we do not include the angular acceleration feedforward input in our control design, and omit its lengthy expression.

As described in Section IV.D, our control design obtains a moment command using INDI. To find the corresponding control inputs, i.e., flap deflections and differential thrust $\Delta T = T_1 - T_2$, we solve (14) for these inputs. We find an expression for the differential thrust ΔT by equating

$$\mathbf{i}_z^{\top} \left(\mathbf{m}_T + \mathbf{m}_{\mu} \right) = \mathbf{i}_z^{\top} \mathbf{m}, \tag{32}$$

which assumes that the contribution by $\mathbf{i}_z^{\top} \mathbf{m}_{\delta}$ is negligible. Due to the multiplication with $\sin \alpha_0$, this assumption typically does not result in significant discrepancies. Using $\mu_1 + \mu_2 = {}^{c_{\mu}}/_{c_T} \Delta T$, we obtain

$$\Delta T = \frac{\mathbf{i}_z^{\top} \mathbf{m}}{l_{T_y} \left(\mathrm{c}\alpha_0 \ \mathrm{c}\bar{\alpha} \ (1 - c_{D_T}) - \mathrm{s}\alpha_0 \ \mathrm{s}\bar{\alpha} \ (c_{L_T} - 1) \right) - \mathrm{s}\alpha_T \ \frac{c_{\mu}}{c_T}}. \tag{33}$$

The individual thrust values are then given by

$$T_1 = \frac{T + \Delta T}{2}, \qquad T_2 = \frac{T - \Delta T}{2}. \tag{34}$$

After obtaining the motor speeds from (6), we can deduct $\mathbf{m}_T$ and $\mathbf{m}_{\mu}$ from $\mathbf{m}$ to obtain $\mathbf{m}_{\delta}$. Finally, the flap deflections are computed by inversion of (13), as follows:

$$\begin{bmatrix} \delta_1 \\ \delta_2 \end{bmatrix} = \begin{bmatrix} -l_{\delta_y} \, \mathrm{c}\alpha_0 \, \mathbf{i}_z^{\top} \boldsymbol{\nu}_1 & l_{\delta_y} \, \mathrm{c}\alpha_0 \, \mathbf{i}_z^{\top} \boldsymbol{\nu}_2 \\ l_{\delta_x} \mathbf{i}_z^{\top} \boldsymbol{\nu}_1 & l_{\delta_x} \mathbf{i}_z^{\top} \boldsymbol{\nu}_2 \end{bmatrix}^{-1} \begin{bmatrix} \mathbf{i}_x^{\top} \mathbf{m}_{\delta} \\ \mathbf{i}_y^{\top} \mathbf{m}_{\delta} \end{bmatrix} \tag{35}$$

with

$$\boldsymbol{\nu}_i = -c_{L_T}^{\delta} \cos \bar{\alpha} \ T_i - c_{L_V}^{\delta} \| \mathbf{v} \| \mathbf{i}_x^{\top} \mathbf{v}^{\alpha}. \tag{36}$$

IV. Trajectory-tracking Control

Our proposed controller is designed to accurately track the dynamic position reference $\boldsymbol{\sigma}_{\mathrm{ref}}$. It consists of several components based on various control methodologies, as shown in Table 1. Each component employs a global formulation that enables seamless maneuvering throughout the flight envelope. By separating kinematics and dynamics, we are able to employ proportional-derivative (PD) control on the translational and rotational kinematics. Application of the resulting linear and angular acceleration commands is performed using INDI control. INDI enables accurate control by incremental adjustment of control inputs, based on the inverted dynamics model derived in Section III. Due to its incremental formulation, the controller only depends on local accuracy of the input-output relation, resulting in favorable robustness against modeling errors and external disturbances. As we will detail in this section, these errors and disturbances (i.e., $\mathbf{f}_{\mathrm{ext}}$ and $\mathbf{m}_{\mathrm{ext}}$) are implicitly estimated and corrected for based on the difference between sensor-based and model-based force and moment estimates. By directly incorporating linear and angular acceleration measurements to obtain the sensor-based estimates, the controller is able to quickly and wholly counteract errors and disturbances, without relying on integral action.

Our proposed control design uses a state estimate consisting of position $\mathbf{x}$, velocity $\mathbf{v}$, and attitude $\boldsymbol{\xi}$. Additionally, linear acceleration $\mathbf{a}$ and angular velocity $\boldsymbol{\Omega}$ measurements in the body-fixed reference frame are obtained from an inertial measurement unit (IMU). Motor speeds $\boldsymbol{\omega}$ and flap deflections $\boldsymbol{\delta}$ are measured and utilized as well.

Table 1 Overview of trajectory-tracking controller components.

Component	Methodology	Reference	Control Output	Description
Position and Velocity Control	PD	$\mathbf{x}_{\text{ref}}$, $\mathbf{v}_{\text{ref}}$, $\mathbf{a}_{\text{ref}}$	$\mathbf{a}_c$	Section IV.A
Linear Acceleration Control	INDI	$\mathbf{a}_c$, ψ_{ref}	$\boldsymbol{\xi}_c$, T_c	Section IV.B
Attitude and Angular Rate Control	PD	$\boldsymbol{\xi}_c$, $\mathbf{j}_{\text{ref}}$, $\dot{\psi}_{\text{ref}}$	$\dot{\boldsymbol{\Omega}}_c$	Section IV.C
Angular Acceleration Control	INDI	$\dot{\boldsymbol{\Omega}}_c$	$\boldsymbol{\omega}_c$, $\boldsymbol{\delta}_c$	Section IV.D
Motor Speed Control	Integrative	$\boldsymbol{\omega}_c$	$\boldsymbol{\zeta}$	Section IV.E

A. PD Position and Velocity Control

We use cascaded proportional-derivative (PD) controllers for position and velocity control, resulting in the following expression for the acceleration command:

$$\mathbf{a}_c = \mathbf{R}_b^i \left(\mathbf{K}_{\mathbf{x}} \mathbf{R}_i^b \left(\mathbf{x}_{\text{ref}} - \mathbf{x} \right) + \mathbf{K}_{\mathbf{v}} \mathbf{R}_i^b \left(\mathbf{v}_{\text{ref}} - \mathbf{v} \right) + \mathbf{K}_{\mathbf{a}} \mathbf{R}_i^b \left(\mathbf{a}_{\text{ref}} - \tilde{\mathbf{a}}_{\text{lpf}} \right) \right) + \mathbf{a}_{\text{ref}} \tag{37}$$

with $\mathbf{K}_\bullet$ indicating diagonal gain matrices. The first term of (37) aims to null the position and velocity errors, while the second term is a feedforward input that ensures the acceleration reference is accurately tracked. Since the vehicle has different acceleration capabilities along its body-fixed axes, we define the control gains in the body-fixed reference frame and transform them to the world-fixed frame for each control update.

The gravity-corrected linear acceleration in the inertial reference frame is obtained as

$$\mathbf{a}_{\text{lpf}} = (\mathbf{R}_b^i \mathbf{a}^b + g \mathbf{i}_z)_{\text{lpf}}, \tag{38}$$

where lpf indicates low-pass filtering that is applied to IMU measurements to alleviate measurement noise, e.g., due to vibrations. We follow the method by [25] and deduct acceleration contributions due to the transient flap movements. This correction helps eliminate pitch oscillations that may result from the non-minimum phase response of acceleration to flap deflections. To isolate transient movement, we first filter the measured flap deflections using the low-pass filter and then using a high-pass filter, resulting in a band-pass filtered signal. The low-pass filter helps to match the phase delay between accelerometer and flap deflection measurements, and ensures that we do not (re-)introduce high-frequency noise in the resulting acceleration signal

$$\tilde{\mathbf{a}}_{\text{lpf}} = \mathbf{a}_{\text{lpf}} - m^{-1} \mathbf{R}_a^i \mathbf{f}_{\delta_{\text{hpf}}}^a. \tag{39}$$

B. INDI Linear Acceleration Control

INDI control incrementally updates the attitude and collective thrust to track the acceleration command $\mathbf{a}_c$. The controller estimates the unmodeled force $\mathbf{f}_{\text{ext}}$ by comparing the measured acceleration to the expected acceleration according to the vehicle aerodynamics model and motor speed measurements. By rewriting (2), we obtain

$$\mathbf{f}_{\text{ext}} = m \left(\tilde{\mathbf{a}}_{\text{lpf}} - g \mathbf{i}_z \right) - \mathbf{R}_\alpha^i \mathbf{f}_{\text{lpf}}^\alpha, \tag{40}$$

where, for consistency with $\tilde{\mathbf{a}}_{\text{lpf}}$, low-pass filtered motor speeds and the filtered flap deflections without transient component are used in the computation of $\mathbf{f}_{\text{lpf}}^\alpha$ according to (9). Substitution of (40) into (2) gives

$$\begin{aligned} \mathbf{a} &= g \mathbf{i}_z + m^{-1} \left(\mathbf{R}_\alpha^i \mathbf{f}^\alpha + \mathbf{f}_{\text{ext}} \right) \\ &= g \mathbf{i}_z + m^{-1} \left(\mathbf{R}_\alpha^i \mathbf{f}^\alpha + \left(m \left(\tilde{\mathbf{a}}_{\text{lpf}} - g \mathbf{i}_z \right) - \mathbf{R}_\alpha^i \mathbf{f}_{\text{lpf}}^\alpha \right) \right) \\ &= \tilde{\mathbf{a}}_{\text{lpf}} + m^{-1} \left(\mathbf{f}^i - \mathbf{f}_{\text{lpf}}^i \right). \end{aligned} \tag{41}$$

Solving (41) for $\mathbf{f}^i$ gives an incremental expression for the force command that corresponds to the commanded acceleration, as follows:

$$\mathbf{f}_c^i = m(\mathbf{a}_c - \tilde{\mathbf{a}}_{\text{lpf}}) + \mathbf{f}_{\text{lpf}}^i. \tag{42}$$

This incremental control law enables the controller to achieve the commanded acceleration despite potential modeling discrepancies and external forces, without depending on integral action. If the commanded acceleration is not yet

attained, the force command will be adjusted further in subsequent control updates until the first term in (42) vanishes. Based on the force command $\mathbf{f}_c^i$, the commanded attitude $\boldsymbol{\xi}_c$ is obtained from ψ_{ref}, (17) and (21), and the collective thrust command T_c is obtained from (22). Note that it is through the flatness transform described in Section III that our INDI algorithm can perform fully nonlinear inversion, without linearization of the dynamics in (41). The nonlinear inversion provides more accurate control commands when large acceleration deviations occur, such as may happen during aggressive maneuvers with quickly changing acceleration references.

C. PD Attitude and Angular Rate Control

Given the extensive attitude envelope of the tailsitter vehicle, our attitude controller employs quaternion representation to avoid kinematic singularities. The attitude error quaternion is obtained as

$$\boldsymbol{\xi}_e = \boldsymbol{\xi}^{-1} \circ \boldsymbol{\xi}_c, \tag{43}$$

the corresponding three-element error angle vector is given by

$$\boldsymbol{\zeta}_e = \frac{2 \arccos \xi_e^w}{\sqrt{1 - \xi_e^w \xi_e^w}} \begin{bmatrix} \xi_e^x & \xi_e^y & \xi_e^z \end{bmatrix}^\top. \tag{44}$$

The angular acceleration command is obtained using the PD controller

$$\dot{\boldsymbol{\Omega}}_c = \mathbf{K}_{\boldsymbol{\xi}} \boldsymbol{\zeta}_e + \mathbf{K}_{\boldsymbol{\Omega}} \left(\boldsymbol{\Omega}_{\text{ref}} - \boldsymbol{\Omega}_{\text{lpf}} \right), \tag{45}$$

where $\boldsymbol{\Omega}_{\text{lpf}}$ is the low-pass filtered angular velocity measurement from the IMU, and $\boldsymbol{\Omega}_{\text{ref}}$ is the feedforward angular velocity reference obtained by (31) based on $\dot{\psi}_{\text{ref}}$ and $\mathbf{j}_{\text{ref}}$. By including this feedforward jerk term, the controller improves trajectory-tracking accuracy, especially on agile trajectories with fast-changing acceleration references.

D. INDI Angular Acceleration Control

The angular acceleration controller has a similar construction as its linear acceleration counterpart described in Section IV.B. By rewriting (4), we obtain the following expression for the unmodeled moment:

$$\mathbf{m}_{\text{ext}} = \mathbf{J}\dot{\boldsymbol{\Omega}}_{\text{lpf}} - \mathbf{m}_{\text{lpf}} + \boldsymbol{\Omega}_{\text{lpf}} \times \mathbf{J}\boldsymbol{\Omega}_{\text{lpf}}, \tag{46}$$

where $\dot{\boldsymbol{\Omega}}_{\text{lpf}}$ is obtained by numerical differentiation of $\boldsymbol{\Omega}_{\text{lpf}}$, and $\mathbf{m}_{\text{lpf}}$ is calculated using (14) and based on the low-pass filtered flap deflection and motor speed measurements. Substitution of (46) into (4) gives

$$\begin{aligned} \dot{\boldsymbol{\Omega}} &= \mathbf{J}^{-1} \left(\mathbf{m} + \mathbf{m}_{\text{ext}} - \boldsymbol{\Omega} \times \mathbf{J}\boldsymbol{\Omega} \right) \\ &= \mathbf{J}^{-1} \left(\mathbf{m} + \left(\mathbf{J}\dot{\boldsymbol{\Omega}}_{\text{lpf}} - \mathbf{m}_{\text{lpf}} + \boldsymbol{\Omega}_{\text{lpf}} \times \mathbf{J}\boldsymbol{\Omega}_{\text{lpf}} \right) - \boldsymbol{\Omega} \times \mathbf{J}\boldsymbol{\Omega} \right) \\ &= \dot{\boldsymbol{\Omega}}_{\text{lpf}} + \mathbf{J}^{-1} \left(\mathbf{m} - \mathbf{m}_{\text{lpf}} \right), \end{aligned} \tag{47}$$

where it is assumed that the angular momentum term is relatively slow changing, so that the difference with its filtered version may be neglected. Solving (47) for $\mathbf{m}$ gives the incremental control law

$$\mathbf{m}_c = \mathbf{J}(\dot{\boldsymbol{\Omega}}_c - \dot{\boldsymbol{\Omega}}_{\text{lpf}}) + \mathbf{m}_{\text{lpf}}. \tag{48}$$

Based on the commanded moment $\mathbf{m}_c$, the thrust and flap deflection commands can now be calculated by (33) and (34), and (35), respectively. Finally, the commanded motor speeds $\boldsymbol{\omega}_c$ are calculated by inversion of (6).

E. Integrative Motor Speed Control

While the flaps are driven by servos equipped with closed-loop position control, the propellers are driven by brushless motors that cannot directly track motor speed commands. Instead, we use the second-order polynomial p to find the corresponding throttle input. This function was obtained from regression analysis of static test data relating motor speed to throttle input. We add integral action to account for changes due to the fluctuating battery voltage, so that the throttle command that is sent to the motor electronic speed controller (ESC) is obtained as

$$q_i = p(\omega_{i,c}) + k_{I_\omega} \int \omega_{i,c} - \omega_i \ \ dt. \tag{49}$$

V. Experimental Results

In this section, we evaluate controller performance on various trajectories that include challenging flight conditions, such as large accelerations, transition on curved trajectories, and uncoordinated flight. A video of the experiments can be found at `https://youtu.be/tGQO-6DPT1M`.

A. Experimental Setup

Experiments were performed in an 18 m × 8 m indoor flight space using the tailsitter vehicle shown in Fig. 1 and described in [27]. The vehicle is 3D-printed using Onyx filament with carbon fiber reinforcement. It weighs 0.7 kg and has a wingspan of 55 cm from tip to tip. It is equipped with two T-Motor F40 2400 KV motors with Gemfan Hulkie 5055 propellers. The motor speeds are measured using optical encoders at one measurement per rotation, i.e., at about 200 Hz in hover. MKS HV93i micro servos are used to control the flaps. We obtain the flap deflection measurement as an analog signal by connecting a wire to the potentiometer in the servo.

The flight control algorithm runs onboard on an STM32 microcontroller using custom firmware. The microcontroller has a clock speed of 400 MHz and takes 25 μs to compute a control update at 32-bit floating point precision. Accelerometer and gyroscope measurements are obtained from an Analog Devices ADIS16475-3 IMU at 2000 Hz, and control updates are performed at the same frequency. Position and attitude measurements are provided by a motion capture tracking system at 360 Hz and sent to the vehicle over Wi-Fi with an average latency of 18 ms.

The IMU, motor speed, and flap deflection measurements are filtered using a second-order Butterworth low-pass filter with cutoff frequency of 15 Hz. The transient flap deflections are obtained by subsequent filtering using a second-order Butterworth high-pass filter with cutoff frequency of 1 Hz. The latency of motion caption data is corrected for by forward propagation of IMU measurements.

B. Lemniscate Trajectory

Figure 4 shows experimental results for tracking of a Lemniscate of Bernouilli with a constant speed of 6 m/s. Throughout the trajectory, ψ_{ref} is set perpendicular to the velocity, leading to coordinated flight. The reference and flown trajectories over eight consecutive laps (of 7 s each) starting at the y extreme are shown in Fig. 4a. It can be seen that the tracking performance is very consistent between laps. Figure 4b shows that the largest position deviation occurs at the end of the circular parts where the vehicle does not fully maintain the reference acceleration of almost 2 g, as can be seen in Fig. 4d. Over the middle part of the trajectory, the vehicle increases speed to catch up (see Fig. 4c), and the position error is reduced again. Overall, the controller achieves a position tracking error of 17 cm root mean square (RMS) with a maximum error of 33 cm.

Figure 4e shows the commanded and flown attitude. The attitude controller uses quaternion representation, but to ease interpretation the figure uses the ZXY Euler angles described in Section III. For this trajectory, ϕ corresponds to the bank angle and reaches almost 1 rad, which matches the acceleration nearing 2 g in Fig. 4d. The maximum attitude error occurs during a small period in the turn, where the vehicle incurs a pitch error of 6 deg. Controlling the pitch angle of a flying wing during aggressive maneuvers is generally challenging due to the lack of an elevator, and the pitch deviation is likely the cause of the relatively large position deviation at the exit of the turn. Overall, the controller is able to track the dynamic attitude command well and it maintains an attitude error of less than 2 deg on each axis during the rest of the trajectory.

C. Knife Edge Transitioning Flight

Our proposed algorithm is able to control the vehicle in uncoordinated flight conditions where it has significant lateral velocity. In knife edge flight, the wingtip is pointing in the velocity direction, leading to roll instability due to the location of the center of gravity behind the quarter span point [25]. Figure 5 shows experimental results for a trajectory where ψ_{ref} is set to enforce knife edge flight on one side and coordinated flight on the other side. The results show that our controller is able to stabilize the knife edge flight condition, and that it is able to transition between knife edge and coordinated flight while at the same time performing a 1.6 g turn.

One lap of the oval trajectory takes 6.25 s to complete at a constant speed of 6 m/s. Referring to the view from above in Fig. 5a, the trajectory is flown in clockwise direction with the straight at the top in knife edge configuration and the straight at the bottom in coordinated flight. During each turn, the yaw reference is rotated by $\pi/2$ rad to enforce the switch between configurations. Consequently, the coordinated flight segment is flown in inverted orientation every other lap. Figure 5a shows the reference and flown position over eight successive laps, and Fig. 5b and Fig. 5c show data

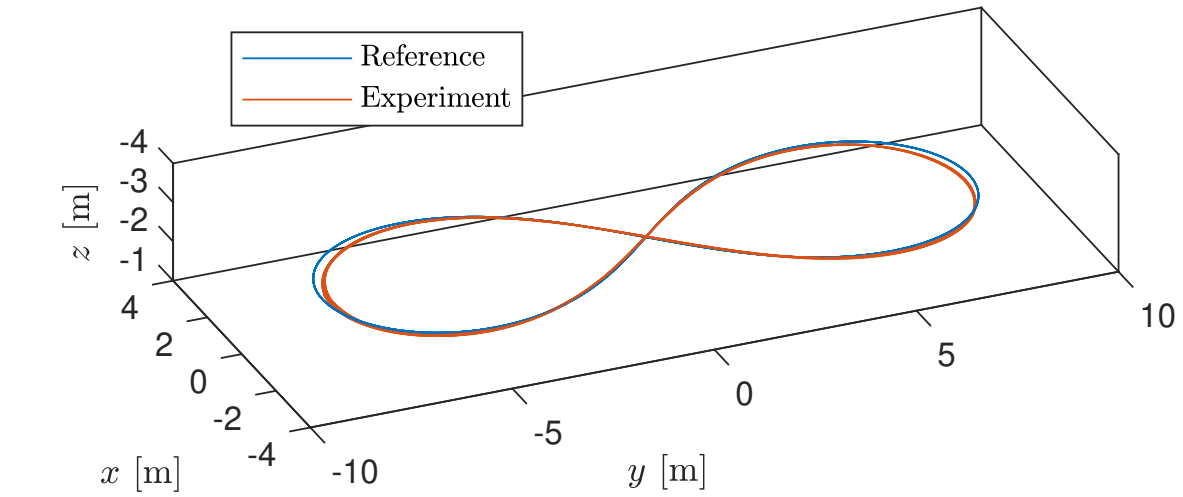

(a) Position.

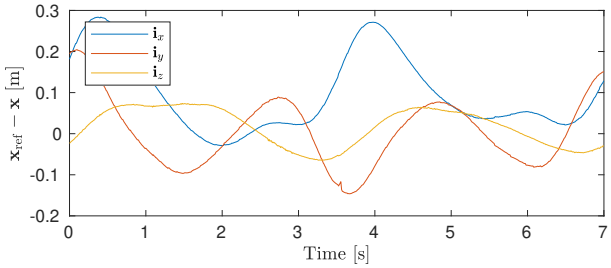

(b) Position tracking error.

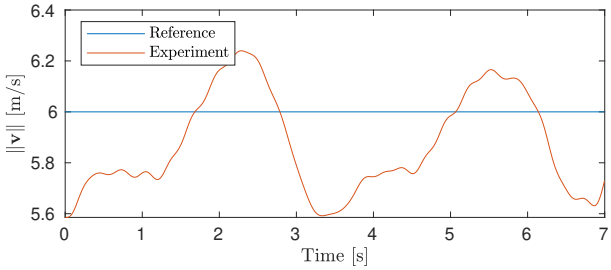

(c) Speed.

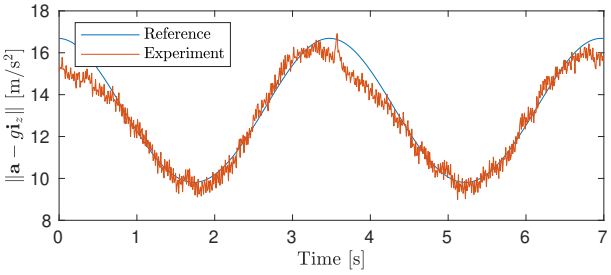

(d) Acceleration.

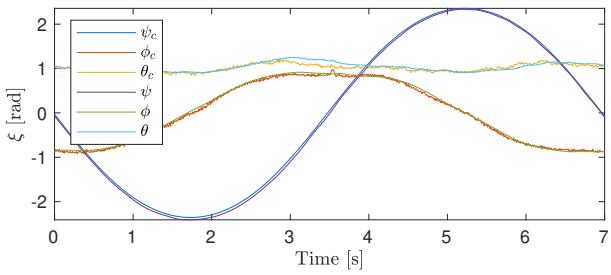

(e) Attitude.

Fig. 4 Experimental results for lemniscate trajectory at 6 m/s.

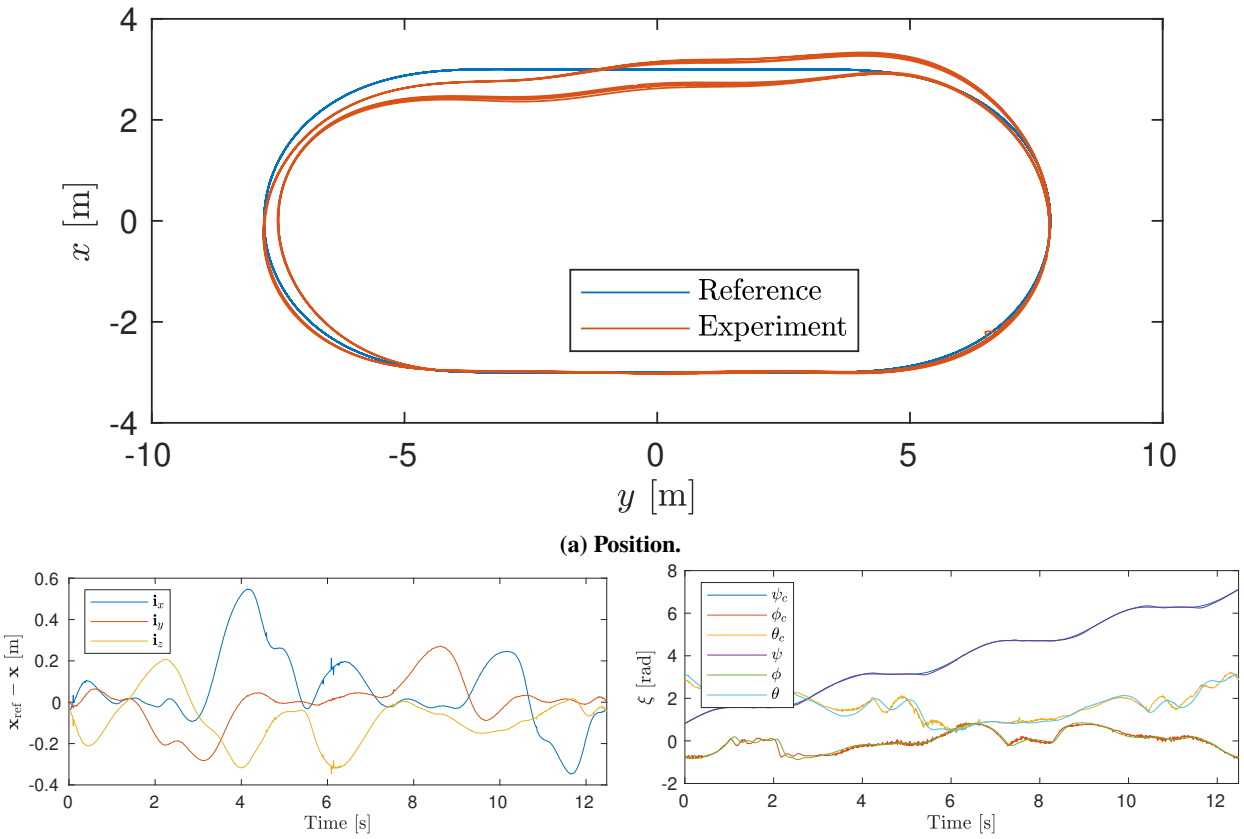

(a) Position.

(b) Position tracking error.

(c) Attitude.

Fig. 5 Experimental results for knife edge transitioning trajectory at 6 m/s.

corresponding to two laps starting and ending at the transition from knife edge flight to coordinated flight in inverted orientation. It can be seen that the reference is followed accurately during both regular and inverted coordinated flight. Even while performing the transition from knife edge to coordinated flight, the controller is able to track the turning trajectory. At the transition from coordinated flight to knife edge, we see that the trajectory is shifted during transitions from inverted orientation. This leads to a position tracking error of at most 60 cm at the start of the knife edge segment. During transition from regular coordinated flight to knife edge a position error of at most 25 cm is incurred.

Flight during the knife edge segment is consistent and stable, and the yaw reference is tracked within 3 deg. In knife edge flight, the vehicle-fixed $\mathbf{b}_z$-axis coincides with the x-axis of Fig. 5a. The position deviation along this axis is due to the fact that the acceleration due to transient movement of the flaps is not considered in the position controller, as described in Section IV.A. The changing acceleration and jerk references result in opposite movement by the flaps at the start and end of the knife edge segment, which is why the turn preceding the knife edge segment is too tight while the turn following it is started not tight enough. Despite this, the controller achieves tracking of the position reference within 26 cm RMS and of the yaw reference within 1.7 deg RMS.

D. Circular Trajectory

Figure 6 shows experimental results for tracking of a circular trajectory reference with a 3.5 m radius at a speed of 8.1 m/s. The left column of figures corresponds to coordinated flight where the $\mathbf{b}_y$-axis is perpendicular to the circle tangent, and the right column corresponds to knife edge flight where the wing tip points along the tangent of the circle. Position tracking performance is very similar between both flights. In both cases, the flown trajectory has a slightly smaller radius than the reference, reducing the flight speed to 7.8 m/s. The RMS position tracking error is 15 cm for both coordinated and knife edge flight. The aircraft reaches a continuous acceleration of 2.1 g. In coordinated flight, this requires a bank angle of 63 deg. In knife edge flight, the aircraft is rolled 14 deg towards the direction of travel to

compensate for drag, and pitched over by 152 deg to provide thrust towards the circle center. Maintaining this state requires flap deflections of 20 deg, and rotor speeds of over 2000 rad/s in knife edge flight. In coordinated flight, the aircraft exploits the lift force to achieve circular flight more efficiently, and requires rotor speeds of 1800 rad/s with flap deflections of 38 deg. In contrast to the trajectory described in Section V.C, the flap deflections are almost constant during the circular trajectory. Hence, there are no transient accelerations caused by the flaps that are not considered in the position controller, and very accurate trajectory tracking is achieved in knife edge flight. This shows that our controller is not only able to stabilize the knife edge flight condition, but also provides accurate trajectory tracking in knife edge flight at speeds close to 8 m/s.

E. Transitions

Figure 7 shows experimental results for transitions between static hover and coordinated flight at 8 m/s on a circular trajectory with 3.5 m radius. Each transition takes 3 s at a constant tangential acceleration of 2.7 m/s^2 and is completed in 12 m. The pitch angle varies over a range of 64 deg. While transitioning from and to hover, the controller tracks the circle trajectory with respectively 10 cm and 15 cm RMS, and 15 cm and 24 cm maximum position error. These maneuvers demonstrate that the controller is capable of performing aggressive transitions while simultaneously tracking turns with significant acceleration.

To evaluate the benefits of the feedforward input based on jerk and yaw rate, we also attempted to fly the same transitions without the angular velocity reference, i.e., with $\boldsymbol{\Omega}_{\text{ref}} = \mathbf{0}$ in (45). We found that the controller is still able to perform 3 s transitions to speeds up to 3 m/s. However, if the target speed is higher and the corresponding tangential acceleration exceeds 1 m/s^2, the absence of the feedforward term causes large deviations from the reference trajectory to the point where the vehicle cannot be stabilized anymore. This confirms the benefit of jerk and yaw rate tracking when flying aggressive maneuvers. Intuitively, the feedforward input enables the control to anticipate future accelerations by regulating not only the forces acting on the vehicle but also their temporal derivative.

F. Differential Thrust Turning

Since the controller is not restricted to coordinated flight, it can perform turns without banking. The tailsitter aircraft is particularly suitable for quick turns using yaw, because of the absence of any vertical surfaces and the availability of relatively powerful motors. Figure 8 shows a fast turn that is executed using differential thrust. The reference trajectory, which is entered in coordinated flight at 7 m/s, changes direction without deviating from a straight line. The controller responds with large differential thrust and flap deflections. At the onset of the turn both flaps are almost fully deflected in opposite directions, and the motors produce a differential thrust of 6.1 N. This causes the aircraft to turn at a maximum rate of 650 deg/s and point in the opposite direction within half a second while remaining within 1 m of the position reference.

VI. Conclusion

In this paper, we presented a control design aimed at tracking agile trajectories using a tailsitter flying wing. We derived a flatness transform for the nonlinear tailsitter flight dynamics with ϕ-theory aerodynamics model, and formulated an angular velocity feedforward input that enables the controller to track the reference position along with its derivatives up to jerk. By applying INDI control, we obtain accurate trajectory tracking without relying on a globally accurate dynamics model. The controller was evaluated in extensive flight experiments were it achieved accurate tracking of challenging trajectories.

Acknowledgments

We thank Murat Bronz and John Aleman for the design, fabrication and assembly of the aircraft, and we thank Lukas Lao Beyer and Nadya Balabanska for the implementation of a flight dynamics simulation tool. This work was supported by the Army Research Office through grant W911NF1910322.

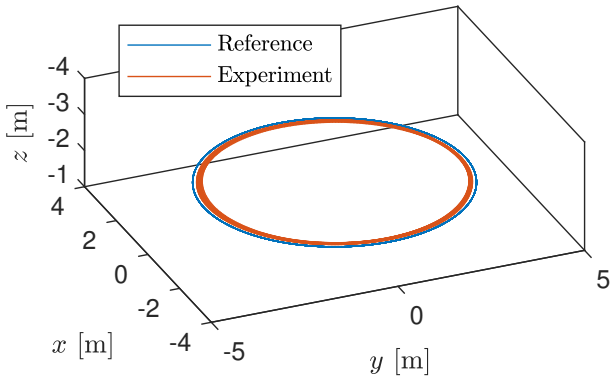

(a) Position.

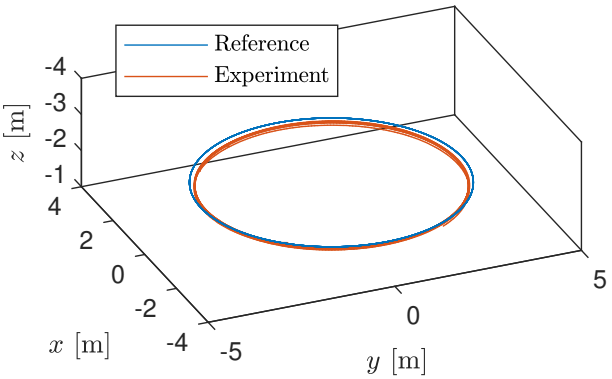

(b) Position.

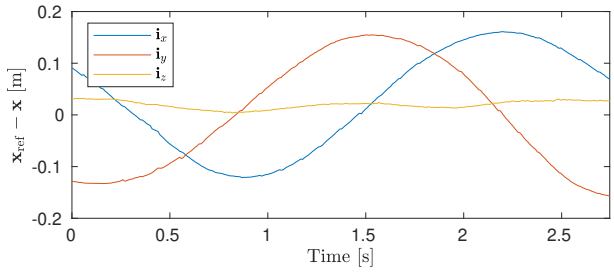

(c) Position tracking error.

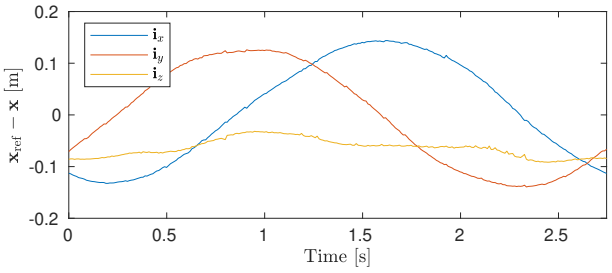

(d) Position tracking error.

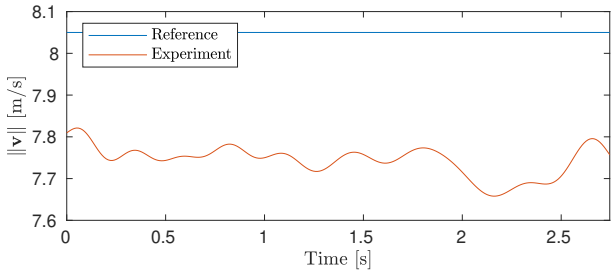

(e) Speed.

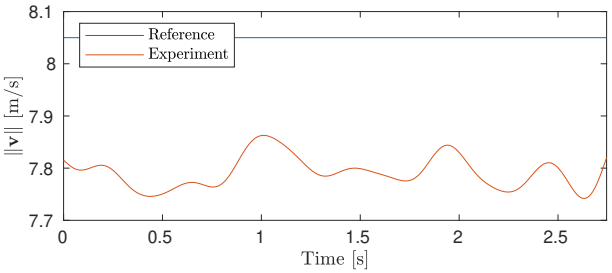

(f) Speed.

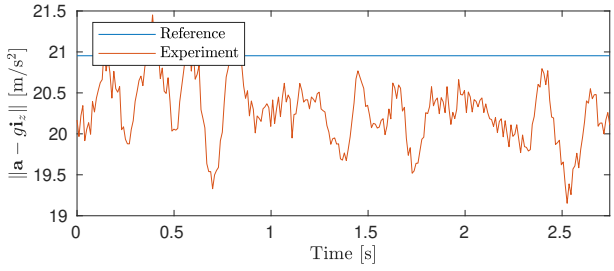

(g) Acceleration.

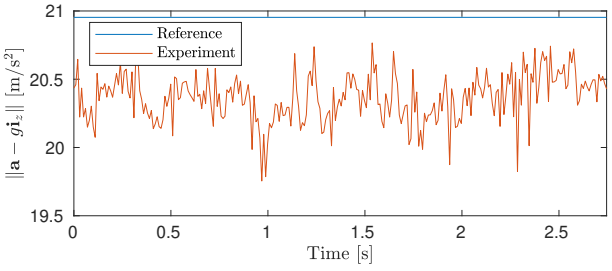

(h) Acceleration.

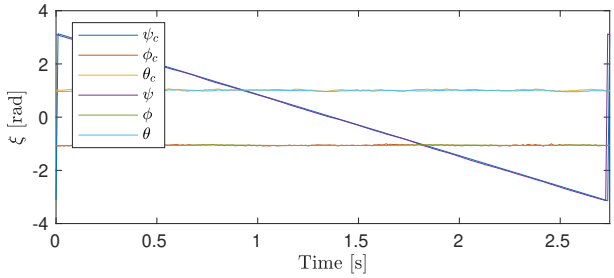

(i) Attitude.

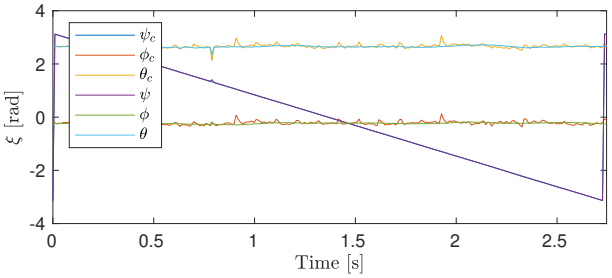

(j) Attitude.

Fig. 6 Experimental results for circle trajectory at 7.8 m/s for coordinated flight in (a), (c), (e), (g), and (i); and for knife edge flight (b), (d), (f), (h), and (j).

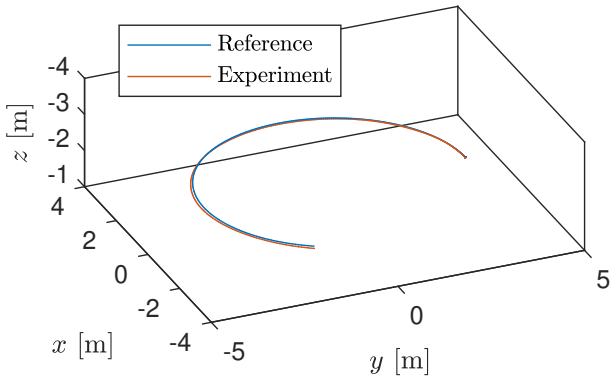

(a) Position.

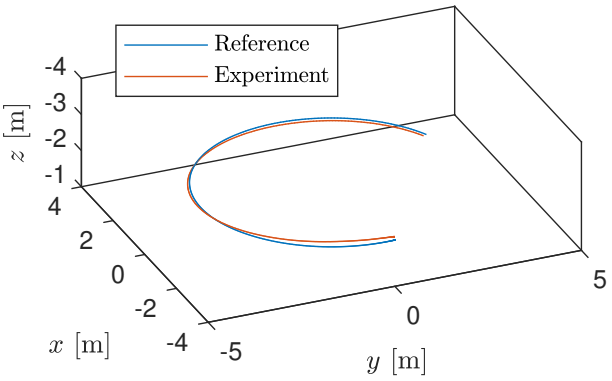

(b) Position.

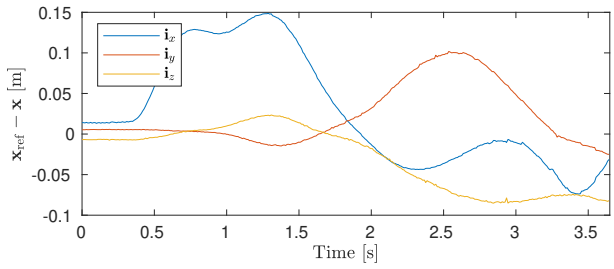

(c) Position tracking error.

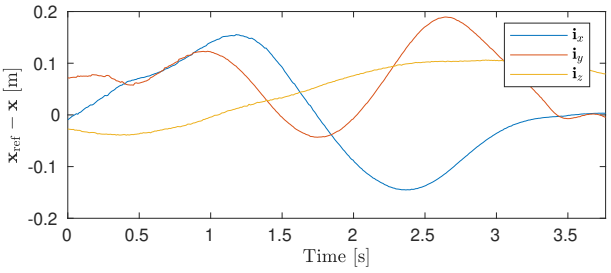

(d) Position tracking error.

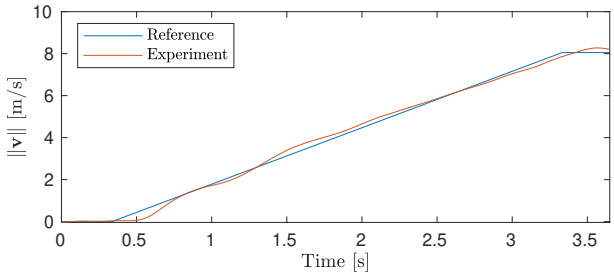

(e) Speed.

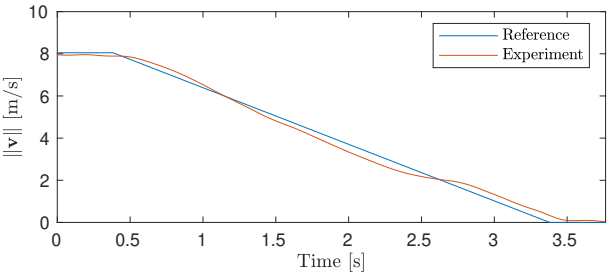

(f) Speed.

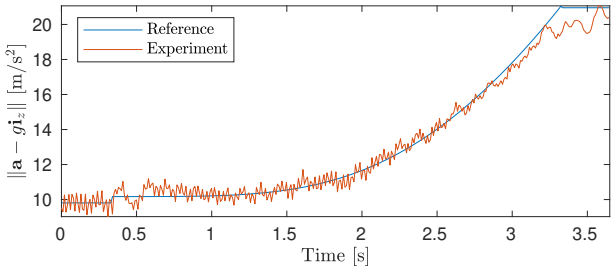

(g) Acceleration.

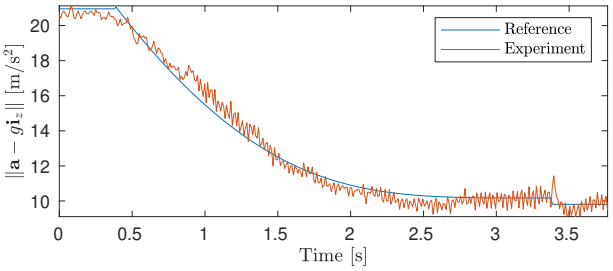

(h) Acceleration.

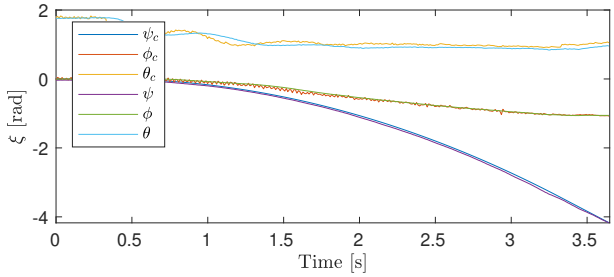

(i) Attitude.

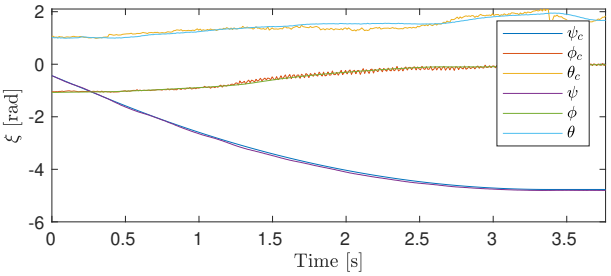

(j) Attitude.

Fig. 7 Experimental results for transition on a circle with radius 3.5 m from static hover to coordinated flight at 8 m/s (a), (c), (e), (g), and (i); and vice versa (b), (d), (f), (h), and (j).

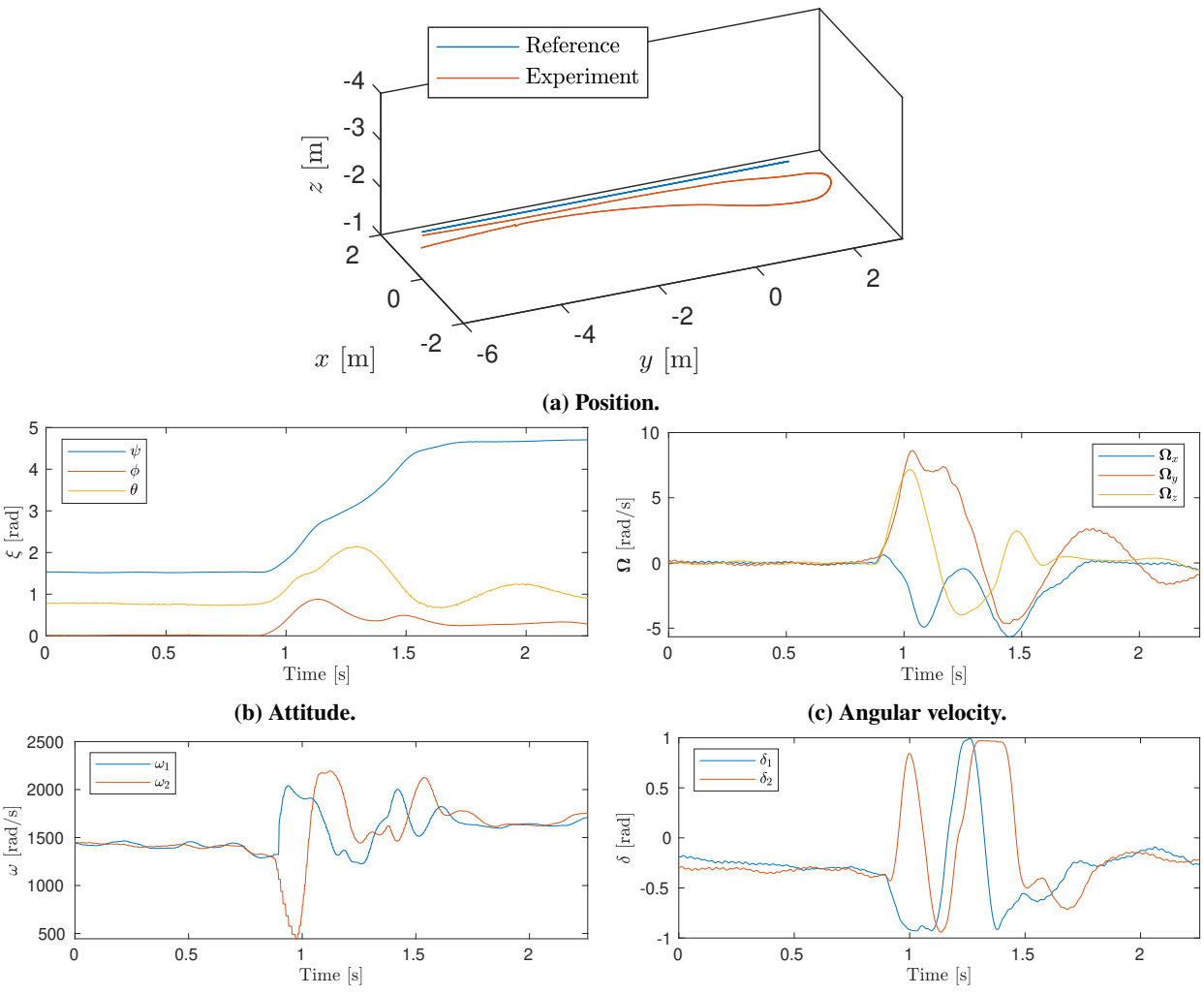

(a) Position.

(b) Attitude.

(c) Angular velocity.

(d) Rotor speed.

(e) Flap deflection.

Fig. 8 Experimental results for differential thrust turn.

References

[1] Lustosa, L. R., Defaÿ, F., and Moschetta, J.-M., "Global singularity-free aerodynamic model for algorithmic flight control of tail sitters," *Journal of Guidance, Control, and Dynamics*, Vol. 42, No. 2, 2019, pp. 303–316.

[2] Fliess, M., Lévine, J., Martin, P., and Rouchon, P., "Sur les systèmes non linéaires différentiellement plats," *CR Acad. Sci. Paris*, 1992, pp. 619–624.

[3] Fliess, M., Lévine, J., Martin, P., and Rouchon, P., "Linéarisation par bouclage dynamique et transformations de Lie-Bäcklund," *Comptes rendus de l'Académie des sciences. Série 1, Mathématique*, Vol. 317, No. 10, 1993, pp. 981–986.

[4] Fliess, M., Lévine, J., Martin, P., and Rouchon, P., "Flatness and defect of non-linear systems: Introductory theory and examples," *International Journal of Control*, Vol. 61, No. 6, 1995, pp. 1327–1361.

[5] Martin, P., "Aircraft control using flatness," *IMACS/IEEE-SMC Multiconference and CESA Symposium on Control, Optimization and Supervision*, 1996, pp. 194–199.

[6] Martin, P., Murray, R. M., and Rouchon, P., "Flat systems, equivalence and trajectory generation," Tech. Rep. 2003.008, California Institute of Technology, 2003.

[7] Ferrin, J., Leishman, R., Beard, R., and McLain, T., "Differential flatness based control of a rotorcraft for aggressive maneuvers," *IEEE/RSJ International Conference on Intelligent Robots and Systems (IROS)*, 2011, pp. 2688–2693.

[8] Rivera, G., and Sawodny, O., "Flatness-Based Tracking Control and Nonlinear Observer for a Micro Aerial Quadcopter," *AIP International Conference on Numerical Analysis and Applied Mathematics (ICNAAM)*, 2010, pp. 386–389.

[9] Faessler, M., Franchi, A., and Scaramuzza, D., "Differential flatness of quadrotor dynamics subject to rotor drag for accurate tracking of high-speed trajectories," *IEEE Robotics and Automation Letters*, Vol. 3, No. 2, 2018, pp. 620–626.

[10] Tal, E., and Karaman, S., "Accurate Tracking of Aggressive Quadrotor Trajectories Using Incremental Nonlinear Dynamic Inversion and Differential Flatness," *IEEE Transactions on Control Systems Technology*, Vol. 29, No. 3, 2021, pp. 1203–1218.

[11] Martin, P., "Contribution à l'étude des systèmes différentiellement plats," Ph.D. thesis, École Nationale Supérieure des Mines de Paris, 1992.

[12] Hauser, J., and Hindman, R., "Aggressive flight maneuvers," *Proceedings of the 36th IEEE Conference on Decision and Control*, Vol. 5, IEEE, 1997, pp. 4186–4191.

[13] Lee, D., Kim, H. J., and Sastry, S., "Feedback linearization vs. adaptive sliding mode control for a quadrotor helicopter," *International Journal of Control, Automation and Systems*, Vol. 7, No. 3, 2009, pp. 419–428.

[14] Smith, P., "A simplified approach to nonlinear dynamic inversion based flight control," *AIAA Atmospheric Flight Mechanics Conference*, 1998, pp. 4461–4469.

[15] Bacon, B., and Ostroff, A., "Reconfigurable flight control using nonlinear dynamic inversion with a special accelerometer implementation," *AIAA Guidance, Navigation, and Control Conference and Exhibit*, 2000, pp. 4565–4579.

[16] Sieberling, S., Chu, Q., and Mulder, J., "Robust flight control using incremental nonlinear dynamic inversion and angular acceleration prediction," *AIAA Journal of Guidance, Control, and Dynamics*, Vol. 33, No. 6, 2010, pp. 1732–1742.

[17] Ke, Y., Wang, K., and Chen, B. M., "Design and implementation of a hybrid UAV with model-based flight capabilities," *IEEE/ASME Transactions on Mechatronics*, Vol. 23, No. 3, 2018, pp. 1114–1125.

[18] Jung, Y., and Shim, D. H., "Development and application of controller for transition flight of tail-sitter UAV," *Journal of Intelligent & Robotic Systems*, Vol. 65, No. 1, 2012, pp. 137–152.

[19] Chiappinelli, R., and Nahon, M., "Modeling and Control of a Tailsitter UAV," *2018 International Conference on Unmanned Aircraft Systems (ICUAS)*, IEEE, 2018, pp. 400–409.

[20] Ritz, R., and D'Andrea, R., "A global controller for flying wing tailsitter vehicles," *2017 IEEE international conference on robotics and automation (ICRA)*, IEEE, 2017, pp. 2731–2738.

[21] Lyu, X., Gu, H., Zhou, J., Li, Z., Shen, S., and Zhang, F., "Simulation and flight experiments of a quadrotor tail-sitter vertical take-off and landing unmanned aerial vehicle with wide flight envelope," *International Journal of Micro Air Vehicles*, Vol. 10, No. 4, 2018, pp. 303–317.

[22] Verling, S., Weibel, B., Boosfeld, M., Alexis, K., Burri, M., and Siegwart, R., "Full attitude control of a VTOL tailsitter UAV," *2016 IEEE international conference on robotics and automation (ICRA)*, IEEE, 2016, pp. 3006–3012.

[23] Barth, J. M., Condomines, J.-P., Bronz, M., Moschetta, J.-M., Join, C., and Fliess, M., "Model-free control algorithms for micro air vehicles with transitioning flight capabilities," *International Journal of Micro Air Vehicles*, Vol. 12, 2020, p. 1756829320914264.

[24] Raab, S. A., Zhang, J., Bhardwaj, P., and Holzapfel, F., "Proposal of a unified control strategy for vertical take-off and landing transition aircraft configurations," *2018 Applied Aerodynamics Conference*, 2018, p. 3478.

[25] Smeur, E. J., Bronz, M., and de Croon, G. C., "Incremental control and guidance of hybrid aircraft applied to a tailsitter unmanned air vehicle," *Journal of Guidance, Control, and Dynamics*, Vol. 43, No. 2, 2020, pp. 274–287.

[26] McIntosh, K., Reddinger, J., Zhao, D., and Mishra, S., "Optimal Trajectory Generation for Transitioning Quadrotor Biplane Tailsitter Using Differential Flatness," *Proceedings of the 77th Vertical Flight Society Annual Forum*, 2021, pp. 386–389.

[27] Bronz, M., Tal, E., Favalli, F., and Karaman, S., "Mission-Oriented Additive Manufacturing of Modular Mini-UAVs," *AIAA Scitech 2020 Forum*, 2020, p. 0064.